Coal fly ash as a secondary source of rare earth elements: mineralogical characterisation, speciation, and alkali roasting pretreatment

Nomsa P. Baloyi*, Tintswalo B.Z. Baloyi

Mineral Processing and Technology Research Centre, Department of Metallurgy, School of Mining, Metallurgy and Chemical Engineering, Faculty of Engineering and the Built Environment, University of Johannesburg, PO Box 524, Auckland Park, Johannesburg 2006, South Africa

* Corresponding author. E-mail address: nbaloyi@uj.ac.za

Abstract

The mineralogical response of coal fly ash (CFA) to alkali roasting is important when assessing its potential as a secondary source of rare earth elements (REEs). A South African CFA containing 60.1 wt% SiO_2, 16.7 wt% Al_2O_3, 10.2 wt% Fe_2O_3 and 6.9 wt% CaO was mixed with Na_2CO_3 (1:1 mass ratio), roasted at 400, 600, 800 and 900 °C for 2 h and water-washed. The feed and washed residues were examined using XRD, SEM-EDX and ICP-MS after HNO_3–HCl–HF microwave digestion; feed XRF established bulk chemistry. The feed contained 414.6 mg/kg detected REY excluding Sc, together with 62.0 mg/kg Sc. Quartz and mullite were identified by XRD. These crystalline phases persisted at 400 and 600 °C, whereas nepheline and carnegieite appeared at 800 °C. At 900 °C, mullite reflections were no longer resolved, quartz reflections were greatly diminished and SEM images showed extensive sintering. ICP-MS measurements showed temperature-dependent differences in element concentrations in the washed residues. The nearly invariant Ce/La ratio suggests similar relative behaviour of these two major REEs across the treatments. The findings establish a strong mineralogical response to Na_2CO_3 at elevated temperatures and identify 900 °C as the preferred pretreatment temperature for subsequent acid leaching.

Keywords: Rare earth elements; Coal fly ash; Sodium carbonate roasting; Nepheline; Process mineralogy; Mode of occurrence

1. Introduction

Rare earth elements (REEs), conventionally the fifteen lanthanides together with yttrium and scandium, are indispensable to permanent magnets, phosphors and catalysts, and demand for them is driven by the transition to low-carbon energy and transport systems (Balaram, 2019). Primary production is geographically concentrated, and the REEs are classified as critical raw

materials by both the European Union and the United States (European Commission, 2020; U.S. DOE, 2017a). This has prompted a sustained search for secondary sources, among which coal and coal combustion products have received particular attention (Seredin and Dai, 2012; Dai and Finkelman, 2018). Because the REEs are essentially non-volatile during pulverised-coal combustion, they are retained and concentrated in the ash; surveys of United States fly ashes report total REE contents that commonly lie between about 400 and 500 mg/kg (Taggart et al., 2016). Seredin and Dai (2012) proposed that coal ashes containing more than about 1000 mg/kg of rare earth oxides merit evaluation as REE raw materials, and emphasised that the proportion of critical elements in the distribution matters as much as the total content.

The question is of practical relevance in South Africa, where coal-fired generation produces about 34 Mt of ash per year, of which only 7–10% is beneficiated (Eskom, 2024). Systematic REE data for South African ashes have appeared only recently. Wagner and Matiane (2018) reported 402–599 mg/kg REY in ashes of selected Main Karoo Basin coals, and Rerani et al. (2024) measured total REE contents exceeding 600 mg/kg in power-station and laboratory ashes. Using mineral liberation analysis, Rerani et al. (2024) identified four REE-bearing phases (monazite, xenotime, a Ce-rich phase and a REE silicate) and found a higher proportion of liberated REE-bearing grains in laboratory ash with less aluminosilicate glass. Cornelius et al. (2021) examined the behaviour of REEs in South African fly ash during wet and magnetic separation and zeolitisation. These studies establish that South African ashes carry a REE inventory comparable to international ashes, but the response of these ashes to chemical pretreatment has received little attention.

Recovery from fly ash is limited less by grade than by the manner in which the REEs are held. Ion microprobe, electron microscopy and selective-dissolution studies show that REEs occur (i) as discrete, typically micrometre-sized phosphate (monazite, xenotime) and oxide grains, which may be free or encapsulated in glass, (ii) dispersed within the aluminosilicate glass, and (iii) in minor association with Fe oxides and other accessory phases such as zircon (Kolker et al., 2017; Pan et al., 2019; Liu et al., 2019; Fu et al., 2022). A distinction is needed between mineral association, which microbeam methods resolve well, and chemical speciation, which they do not quantify. Liu et al. (2019) showed that bulk X-ray absorption spectroscopy and acid leaching of the same Class F ashes gave markedly different apportionments between phosphate, oxide and glass hosts, and concluded that each method yields only indirect estimates that must be cross-validated. The practical consequence is well documented: REE extraction from Class F ash by direct acid leaching is typically incomplete (about 30–70%) and depends

strongly on acid type, concentration, temperature and ash source (Cao et al., 2018; King et al., 2018; Liu et al., 2019).

Alkali roasting or fusion addresses this limitation by converting the acid-resistant mullite–quartz–glass assemblage into acid-soluble sodium silicates and aluminosilicates, thereby exposing the REE hosts to the lixiviant. Taggart et al. (2018) compared six additives at 450 °C and obtained more than 90% REE extraction after NaOH roasting, whereas Na_2CO_3 was much less effective; they attributed this to the roasting temperature lying below the melting point of the carbonate. Tang et al. (2019) applied alkali fusion followed by acid leaching to coal fly ash. For alumina recovery, Liu et al. (2024) showed that Na_2CO_3 roasting at a 1:1 mass ratio and 900 °C nearly completely converted mullite to $NaAlSiO_4$, giving 90.3% Al extraction in H_2SO_4.

Na_2CO_3 is cheaper and less corrosive than NaOH, but its effectiveness depends on temperature: thermodynamically, its reaction with mullite becomes favourable above about 700 K (Liu et al., 2024), but kinetics remain slow until the carbonate approaches its melting point (851 °C). How the REE-hosting assemblage and the REE inventory itself evolve across this sub- to supra-melting range has not been reported systematically, nor has the behaviour of the radiogenic (Th, U) and alkaline-earth (Sr, Ba) elements that accompany the REEs. These elements are important because they reflect the host phases and must be managed in any downstream circuit.

This study examines South African coal fly ash treated with Na_2CO_3 at a 1:1 mass ratio at 400, 600, 800 and 900 °C, followed by water washing. XRF was used for the feed, and XRD, SEM-EDX and ICP-MS after mixed-acid digestion were used to compare the feed and treated products. The objectives were to characterise the feed and measured REE inventory, evaluate the temperature dependence of crystalline and morphological changes, compare the measured concentrations of REEs and associated elements, and assess implications for subsequent extraction.

2. Materials and methods

2.1. Coal fly ash sample and experimental programme

The coal fly ash (CFA) was obtained from a South African coal power station. The as-received sample was homogenised and divided into representative sub-samples for characterisation and roasting. The experimental programme is summarised in Fig. 1, and the sample codes and treatment conditions are given in Table 1.

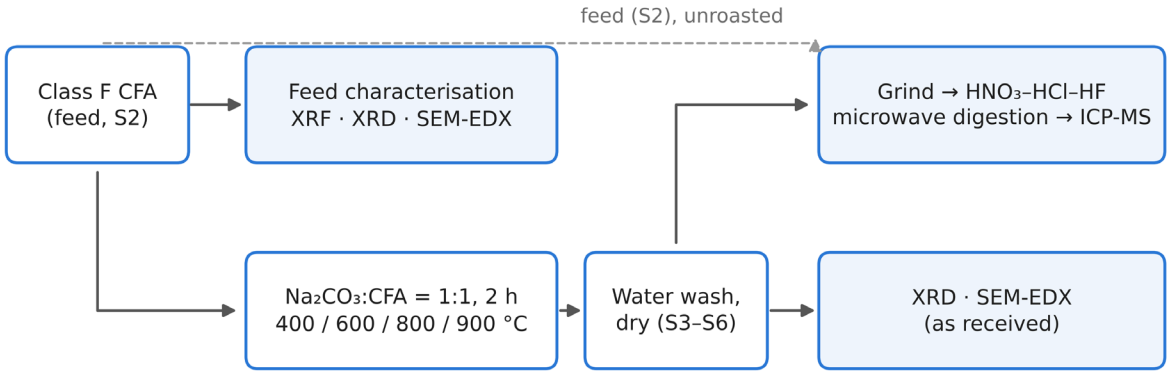

Fig. 1. Experimental programme. The feed (S2) was characterised and digested without roasting; sub-samples were roasted with Na_2CO_3, water-washed and characterised (S3–S6). All ICP-MS samples were ground before digestion.

Table 1. Sample codes and treatment conditions.

Sample code	Description	Roasting temperature (°C)	Na_2CO_3:CFA (mass ratio)	Post-roast treatment
S2	Raw CFA (feed)	–	–	None
S3	Na_2CO_3-roasted CFA	400	1:1	Water-washed
S4	Na_2CO_3-roasted CFA	600	1:1	Water-washed
S5	Na_2CO_3-roasted CFA	800	1:1	Water-washed
S6	Na_2CO_3-roasted CFA	900	1:1	Water-washed

2.2. Sodium carbonate roasting and washing

Anhydrous Na_2CO_3 was mixed with the CFA at a Na_2CO_3:CFA mass ratio of 1:1. Charges of 3 g were placed in crucibles and roasted in a muffle furnace at 400, 600, 800 or 900 °C for 2 h, then cooled to room temperature in the furnace. The calcines were washed with deionised water to remove water-soluble sodium compounds, principally unreacted Na_2CO_3 and sodium silicates formed from excess silica. The residues were recovered by filtration and dried.

2.3. Characterisation

X-ray fluorescence. The bulk chemical composition of the feed was determined on pressed powder pellets using a Rigaku ZSX Primus II wavelength-dispersive XRF spectrometer. Quantification used the standardless SQX fundamental-parameter method in the EZ-scan software, and results are reported as oxides normalised to 100 wt%.

X-ray diffraction. The feed and the washed products were analysed with a Rigaku Ultima IV diffractometer using Cu Kα radiation (λ = 1.5406 Å) at 40 kV and 30 mA with a scintillation counter. Patterns were collected from 5° to 90° 2θ with a step size of 0.02°. Samples were analysed as received, without further grinding. Phases were identified by comparison with the ICDD PDF-4+ database.

Scanning electron microscopy with energy-dispersive X-ray spectroscopy. Particle morphology and composition were examined with a TESCAN VEGA3 scanning electron microscope equipped with an Oxford Instruments energy-dispersive spectrometer using INCA software. Samples were dispersed on carbon tape and coated with carbon. Images were acquired in backscattered-electron (BSE) mode at 20 kV and a working distance of 12.9–13.5 mm, at magnifications of 279–504×. EDX spot analyses and elemental maps were acquired at 20 kV. Spot analyses were quantified as oxides by stoichiometry and normalised to 100 wt%.

2.4. Acid digestion and ICP-MS analysis

Before digestion, the feed and the washed residues were ground to break up agglomerates. Portions of approximately 0.2 g were digested with a mixture of HNO_3, HCl and HF in an Anton Paar microwave digestion system. No visible residue remained after digestion. The digests were diluted to a final volume of 50 mL. Element concentrations were determined with an Agilent 7900 ICP-MS and converted to mass fractions of the digested solid as $w = cV/m$, where c is the solution concentration (mg/L), V the final volume (L) and m the digested mass (kg). Elements below the instrumental detection limit are reported as not detected (nd).

2.5. Data treatment

Element groupings. ΣREE denotes the sum of Sc, Y and the detected lanthanides; ΣREY excludes Sc; and ΣLREE denotes the sum of La, Ce, Pr and Nd (Sm was not detected in any sample). Feed concentrations were normalised to the upper continental crust (UCC) values of Rudnick and Gao (2003).

Mass-balance bounds. Concentrations in the washed products are affected by two opposing mass effects: dilution by Na_2O incorporated into insoluble $NaAlSiO_4$, and enrichment by removal of excess silica as soluble sodium silicate. Bounds were estimated from the feed composition (Table 2) on a basis of 100 g of CFA, assuming that all Al_2O_3 is converted to $NaAlSiO_4$, that all other components are conserved in the residue, and that no sodium is retained other than in $NaAlSiO_4$. Conversion of 16.74 g Al_2O_3 requires $n = 2 \times 16.74/101.96 = 0.328$ mol $NaAlSiO_4$, which incorporates 10.2 g Na_2O and binds 19.7 g SiO_2, leaving 40.4 g of excess SiO_2. The concentration factor f (concentration in the residue divided by that in the feed, for a conserved element) therefore lies between:

$$f(\text{min}) = 100 / (100 + 10.2) = 0.91 \quad \text{(no excess silica removed)} \tag{1}$$

$$f(\text{max}) = 100 / (100 - 40.4 + 10.2) = 1.43 \quad \text{(all excess silica removed)} \tag{2}$$

Changes in concentration between about −9% and +43% relative to the feed can therefore be produced by mass effects alone. The lower bound assumes complete removal of soluble sodium phases during washing; any retained sodium silicate or carbonate would increase the dilution.

Ratio normalisation. Element concentrations were compared with La + Ce as an internal reference to explore relative behaviour across the samples. Such ratios remove the shared concentration scaling factor that arises from changes in residue mass.

$$\Delta_i^* (\%) = 100 \times \{ [c_i/(c(La) + c(Ce))]T / [c_i/(c(La) + c(Ce))]feed - 1 \} \quad (3)$$

where T denotes a roasted product. Δ_i^* is independent of the residue mass. La + Ce was chosen because these are the most abundant and best-quantified REEs in the dataset and their ratio was invariant across all samples (Section 3.5). The normalisation was repeated with Ba as the reference element to test the robustness of the conclusions. A conservative threshold was adopted: values of $|\Delta_i^*|$ below 15% are not interpreted, values of 15–25% are treated as marginal, and only values above 25% are regarded as substantial.

3. Results and discussion

3.1. Physical, chemical and mineralogical characteristics of the feed

3.1.1. Bulk chemistry

The ash is dominated by SiO_2 (60.1 wt%) and Al_2O_3 (16.7 wt%), with substantial Fe_2O_3 (10.2 wt%) and CaO (6.9 wt%) and minor TiO_2, K_2O and MgO (Table 2). The combined SiO_2 + Al_2O_3 + Fe_2O_3 content of 87.0 wt% and the CaO content below 18 wt% classify the ash as Class F (ASTM International, 2025). The SiO_2/Al_2O_3 mass ratio of 3.59 is much higher than that of mullite (0.39) or $NaAlSiO_4$ (1.18). Even if all the Al were present as mullite, that phase could account for at most 23.3 wt% of the ash, so at least 53.5 wt% of the ash, as SiO_2, must reside in quartz and the aluminosilicate glass, the only other Si-bearing components detected. This excess silica governs the roasting chemistry: it can react with Na_2CO_3 to form water-soluble sodium silicate, whereas the Al-bound silica is fixed in insoluble $NaAlSiO_4$ (Section 3.3).

Table 2. Bulk chemical composition of the CFA feed (XRF, pressed powder, standardless SQX, normalised to 100 wt%).

Component	wt%	Component	wt%
SiO_2	60.08	MgO	0.77
Al_2O_3	16.74	SO_3	0.62
Fe_2O_3	10.23	Na_2O	0.14
CaO	6.94	Cr_2O_3	0.13
TiO_2	2.88	MnO	0.10

K_2O	1.14	NiO	0.028
SrO	0.202	Ga_2O_3	0.017
Y_2O_3	0.013		
$SiO_2 + Al_2O_3 + Fe_2O_3$	87.04	SiO_2/Al_2O_3 (mass)	3.59

3.1.2. Crystalline phases

Mullite ($Al_6Si_2O_{13}$) and quartz (SiO_2) were identified as the principal crystalline phases in the feed (Fig. 2). The strongest reflection, near 26.6° 2θ, combines the quartz (101) reflection with overlapping mullite reflections. Although XRF reports 10.2 wt% Fe (as Fe_2O_3), hematite reflections were not resolved. This is consistent with Fe being held in the aluminosilicate glass and in fine-grained or poorly crystalline Fe-rich particles, as indicated by the EDX maps (Fig. 4). The spherical morphology observed by SEM is consistent with a glass-bearing ash.

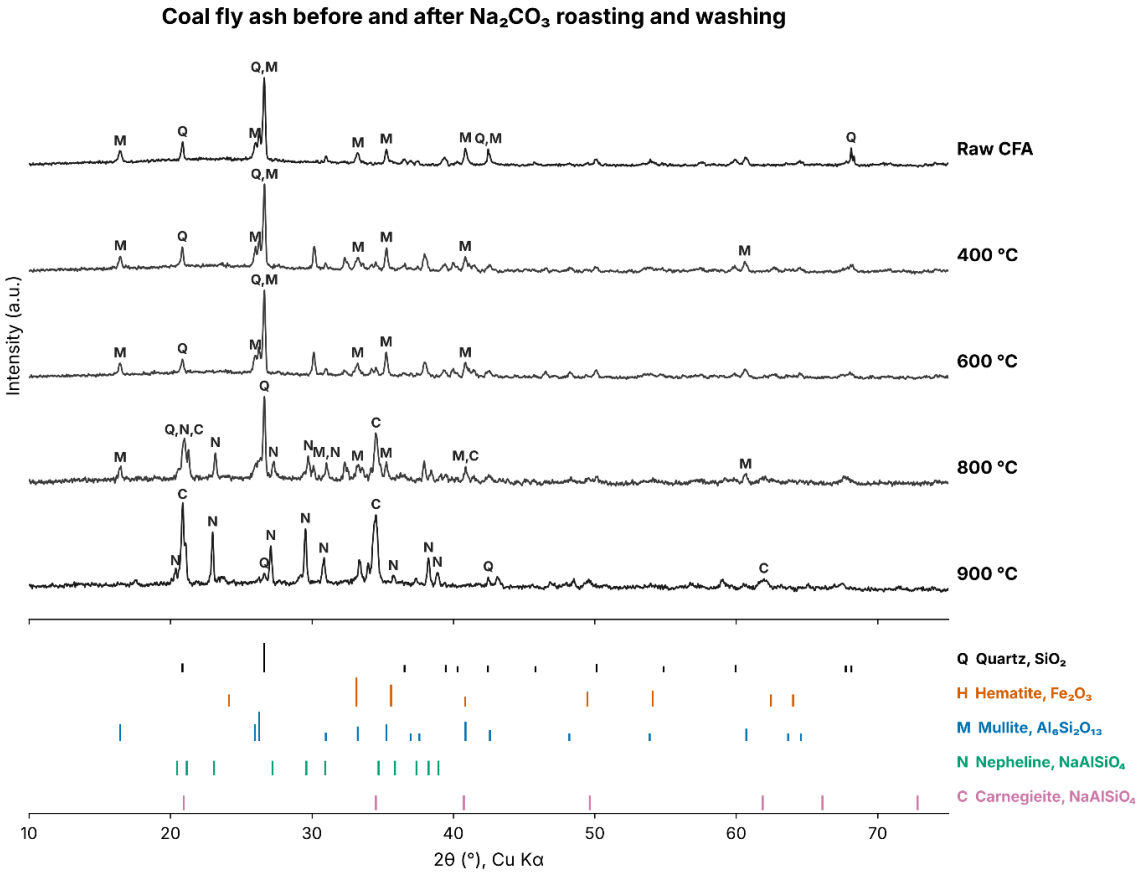

Fig. 2. XRD patterns (Cu Kα) of the feed and of the Na_2CO_3-roasted (1:1) and water-washed products at 400, 600, 800 and 900 °C, with ICDD PDF-4+ reference positions. Q = quartz; M = mullite; N = nepheline; C = carnegieite.

3.1.3. Morphology and microchemistry

The BSE image of the feed (Fig. 3a) shows a dense population of spherical particles, many finer than 20 µm, mixed with irregular and composite particles; a few particles are distinctly brighter in BSE, indicating a higher mean atomic number, typically Fe-rich spheres. Elemental

maps of the feed (Fig. 4) show Si and Al co-located in both the spheres and the irregular particles, consistent with aluminosilicate glass and mullite-bearing material. K and Mg are distributed through the aluminosilicate particles and are concentrated in one large sphere, as expected for a K-bearing glass. Fe occurs as a diffuse signal within the aluminosilicate particles and is enriched in individual spheres and small discrete grains. S is concentrated in small particles and particle rims where it coincides with Ca or K, which suggests sulphate-bearing condensates on particle surfaces, consistent with the 0.62 wt% SO_3 measured by XRF. At bulk concentrations below 0.05 wt%, the REEs are below the detection limit of EDX mapping; micrometre-sized REE grains in South African ashes have been located by targeted bright-phase searches (Rerani et al., 2024).

EDX spot analyses (Table 3) of aluminosilicate particles give Al/Si atomic ratios of 0.49–0.65, considerably higher than the bulk ratio of 0.33 calculated from the XRF data. The analysed particles are therefore Al-rich glass or mullite-bearing material, whereas quartz carries much of the remaining bulk silica. The Na Kα peak (1.04 keV) is absent from the feed spectrum and becomes progressively stronger in the roasted products (Table 3), recording the uptake of sodium during roasting (Section 3.4).

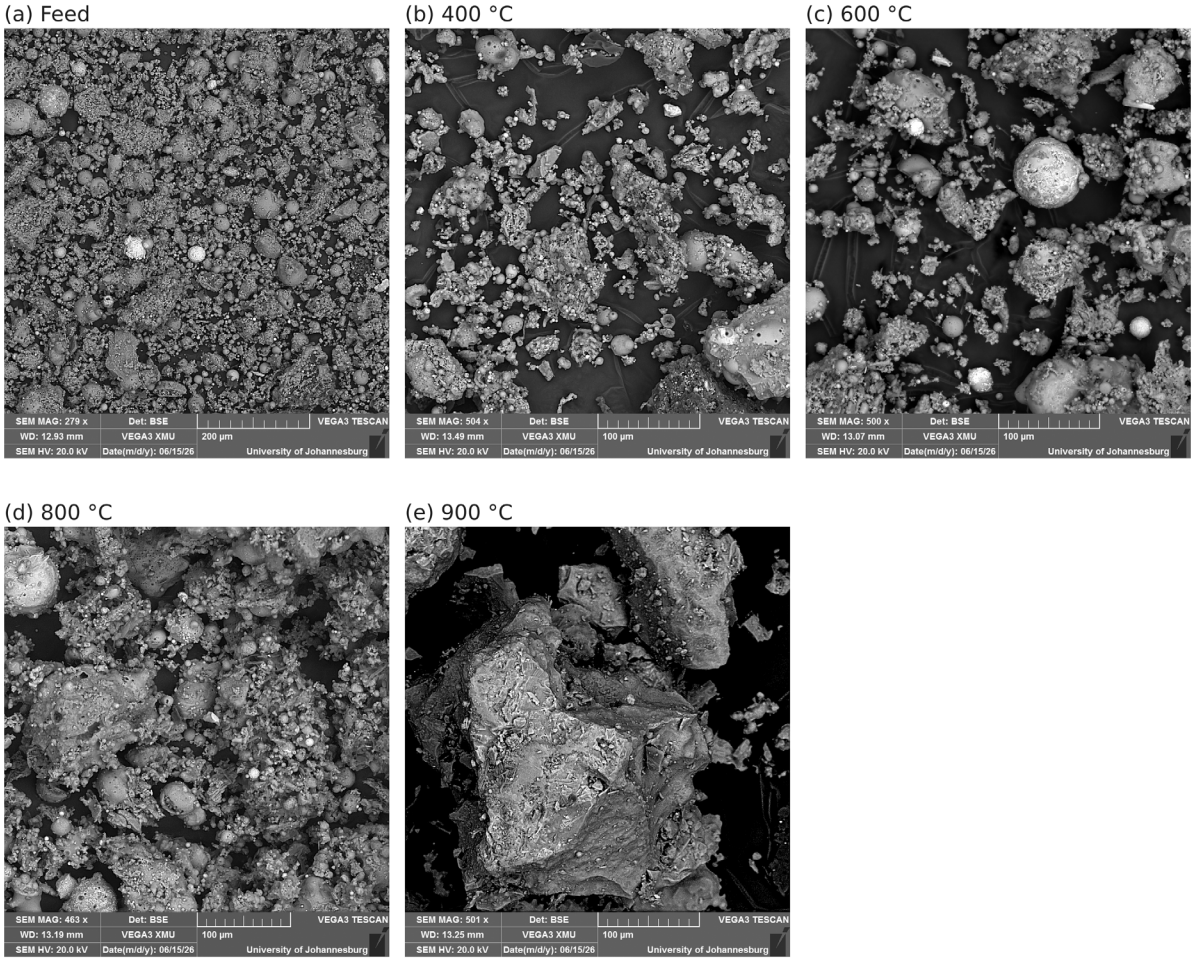

Fig. 3. SEM-BSE images (20 kV) of (a) the feed and the Na_2CO_3-roasted and washed products at (b) 400 °C, (c) 600 °C, (d) 800 °C and (e) 900 °C. Note the lower magnification of (a) (scale bar 200 µm; 100 µm in b–e). Brightness and contrast were adjusted uniformly over each image.

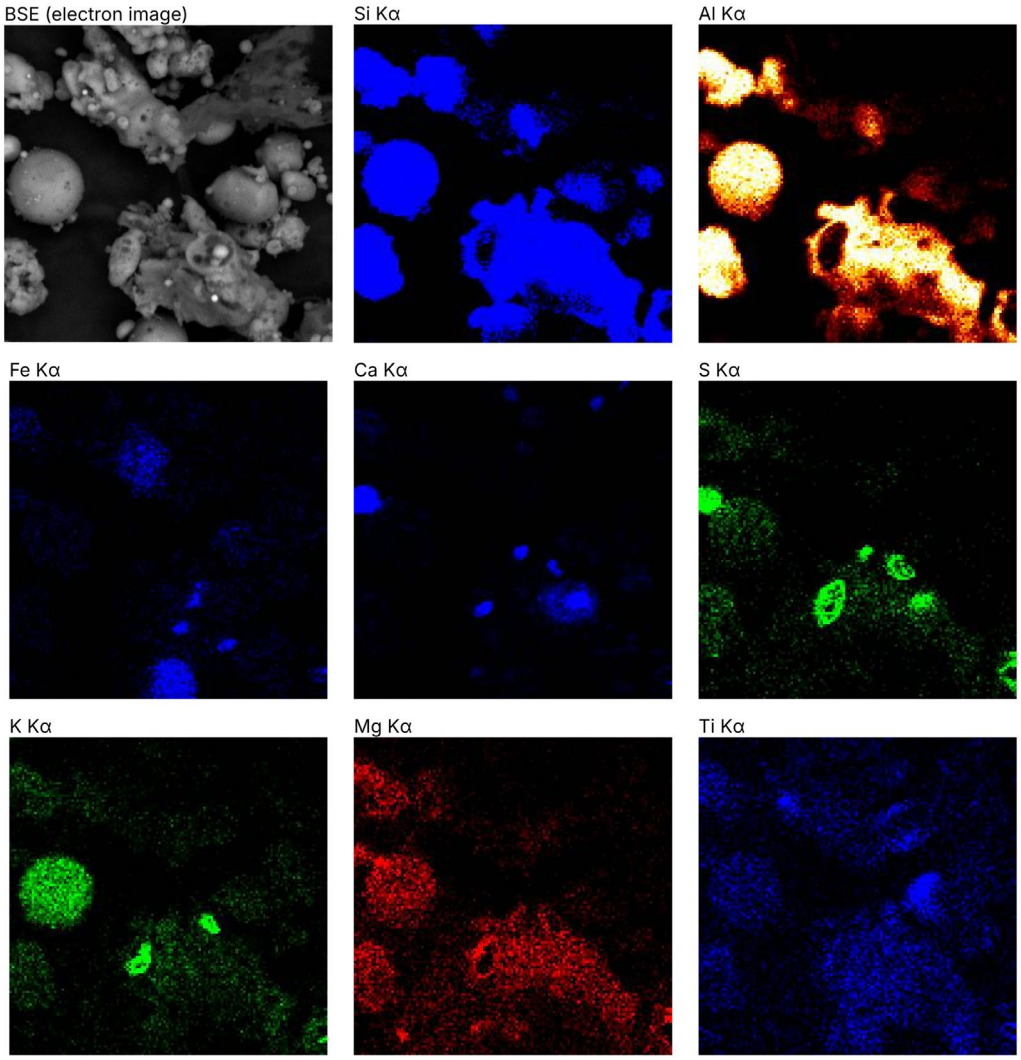

Fig. 4. BSE image and EDX elemental maps (Si, Al, Fe, Ca, S, K, Mg and Ti Kα) of the feed. Colour intensity is qualitative and not comparable between elements.

Table 3. EDX spot analyses of aluminosilicate particles in the feed and the roasted products (wt%, normalised to 100% on a Na-free basis) and relative intensity of the Na Kα peak.

Sample	Al	Si	Ca	Fe	K	Mg	Ti	S	Al/Si (at.)	Na Kα peak
Feed	16.23	26.71	3.21	2.21	0.79	0.34	1.37	0.43	0.63	absent
400 °C	16.67	26.52	2.99	2.53	0.64	0.40	1.34	–	0.65	weak
600 °C	16.46	27.12	3.04	2.10	0.65	0.58	1.30	–	0.63	moderate
800 °C	14.76	25.50	5.24	3.66	0.82	0.85	1.49	0.26	0.60	strong
900 °C	12.81	27.26	5.48	4.12	0.76	1.01	1.16	–	0.49	strong

Cu (0.53 wt%) in spectrum 7, attributed to the sample holder, is excluded.

3.2. REE content and inferred modes of occurrence in the feed

The feed contains 476.6 mg/kg ΣREE, or 414.6 mg/kg ΣREY when Sc is excluded (Table 5). Ce (221.0 mg/kg) and La (94.5 mg/kg) account for 66% of ΣREE, followed by Sc (62.0 mg/kg), Y (47.2 mg/kg) and Nd (44.7 mg/kg). Because Sm, Eu, Tb and Ho–Lu were below detection, ΣREY is a lower bound. The detected inventory lies within the range reported for South African

ashes (402–599 mg/kg REY; Wagner and Matiane, 2018) and is comparable to that of many United States ashes (Taggart et al., 2016). It is below the cut-off of about 1000 mg/kg rare earth oxides proposed by Seredin and Dai (2012), but it exceeds the 300 mg/kg total REE level that the U.S. Department of Energy identified as important for commercially viable extraction from coal-based materials (U.S. DOE, 2017b). Because the detected inventory understates the total REY and South African ash stockpiles are large, the ash merits further evaluation as a secondary REE source, provided that pretreatment improves REE accessibility.

Normalised to the upper continental crust (Fig. 5), the feed is enriched in Sc (4.4×), Ce (3.5×), La (3.1×), Y (2.3×) and Nd (1.7×). Pr (0.62×), Gd (0.27×) and Dy (0.44×), however, appear depleted relative to their neighbours: the La/Pr mass ratio is 21 (UCC ≈ 4.4) and Dy/Y is 0.036 (UCC ≈ 0.19). Normalised REE distributions in coal ash are normally smooth (Seredin and Dai, 2012), and fractionation of this magnitude between adjacent lanthanides is not geochemically plausible. These low values are attributed to the elevated detection limits that follow 250-fold dilution of a 0.2 g sample. Pr, Gd and Dy are therefore treated as semi-quantitative, and critical-REE ratios and the outlook coefficient of Seredin and Dai (2012) are not calculated. The discussion relies on the well-quantified elements La, Ce, Y, Ba, Sr and Th, with Nd and Sc qualified in Section 3.5.

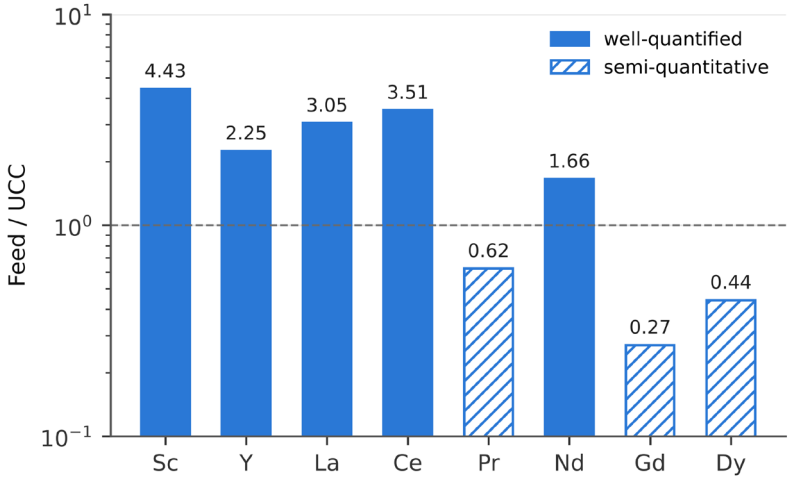

Fig. 5. Concentrations of the detected REEs, Y and Sc in the feed normalised to the upper continental crust (Rudnick and Gao, 2003). Hatched bars denote elements considered semi-quantitative; Sm, Eu, Tb and Ho–Lu were not detected.

The measured REE inventory, XRD phase assemblage and SEM-EDX microchemistry constrain the likely modes of REE occurrence. The feed consists mainly of aluminosilicate glass and mullite, with Fe-rich spheres and grains. Published studies of comparable coal ashes report REEs dispersed in aluminosilicate glass, enclosed in accessory phosphate grains such as

monazite and xenotime, and associated with Fe-bearing phases (Kolker et al., 2017; Pan et al., 2019; Liu et al., 2019; Rerani et al., 2024). The mineralogy of the present ash is consistent with these modes of occurrence, and the feed Th content (28.0 mg/kg) together with its LREE dominance is consistent with a phosphate-hosted LREE–Th fraction. In this paper, speciation refers to these modes of occurrence.

3.3. Phase transformations during Na_2CO_3 roasting

The crystalline phases identified in the washed products are summarised in Table 4 and Fig. 2. Their evolution defines three regimes.

Regime I (400 and 600 °C). The patterns remain dominated by mullite and quartz with relative intensities similar to the feed, and no sodium aluminosilicate was detected. Na_2CO_3 therefore did not react appreciably with the crystalline aluminosilicates at these temperatures.

Regime II (800 °C). Nepheline and carnegieite (both $NaAlSiO_4$) appear alongside mullite and quartz. Quartz reflections remain strong, but mullite reflections are weaker, showing that the reaction of Na_2CO_3 with the aluminosilicate framework begins below the melting point of Na_2CO_3 (851 °C). This agrees with thermodynamic analysis showing that the reaction with mullite becomes favourable well below the melting point (Liu et al., 2024); at 800 °C its extent is limited by solid-state diffusion at particle contacts.

Regime III (900 °C). Mullite is no longer detected, quartz is reduced to weak residual reflections, and nepheline and carnegieite dominate the pattern. Conversion of the crystalline aluminosilicates is essentially complete, in agreement with the near-complete destruction of mullite reported by Liu et al. (2024) for Na_2CO_3 roasting at 900 °C and a 1:1 ratio. The strongest reflection, near 21.0° 2θ (d ≈ 4.2 Å), is assigned to carnegieite; the principal reflection of α-cristobalite would lie near 22.0° 2θ (d ≈ 4.04 Å) and is not observed. Carnegieite, the high-temperature $NaAlSiO_4$ polymorph, coexists with nepheline, which is consistent with rapid crystallisation from a reactive, partly molten system. No crystalline sodium silicate or Na_2CO_3 was detected in the washed 900 °C product, and no Ca-bearing silicate (e.g. gehlenite) was identified despite 6.9 wt% CaO.

At 900 °C, the measured XRD patterns indicate extensive conversion of the detectable crystalline mullite and quartz assemblage and the appearance of sodium aluminosilicate phases.

Table 4. Crystalline phases identified by XRD in the feed and the Na_2CO_3-roasted and washed products.

Phase	Formula	Feed	400 °C	600 °C	800 °C	900 °C

Quartz	SiO_2	✓	✓	✓	✓ (strong)	weak, residual
Mullite	$Al_6Si_2O_{13}$	✓	✓	✓	✓ (weaker)	–
Nepheline	$NaAlSiO_4$	–	–	–	✓	✓ (major)
Carnegieite	$NaAlSiO_4$	–	–	–	✓	✓ (major)
Hematite	Fe_2O_3	not resolved	not resolved	not resolved	not resolved	not resolved

✓ = identified; – = not detected.

3.4. Morphological evolution during roasting

The BSE images (Fig. 3b–e) show a progressive change in morphology with temperature that parallels the phase evolution. At 400 °C (Fig. 3b), discrete spheres persist alongside irregular particles and loose clusters, and several spheres carry pitted surfaces. At 600 °C (Fig. 3c), the spheres are still intact but have rougher surfaces and adhering fine spherules, and small clusters are common. At 800 °C (Fig. 3d), most of the material is consolidated into agglomerates of about 100 µm and larger, in which spheres are embedded in, and partly fused to, irregular reaction product, although many spheres remain recognisable. At 900 °C (Fig. 3e), the morphology changes fundamentally: the material consists of massive, angular bodies larger than 200 µm with fused surfaces bearing fine angular relief, and only a few residual spheres remain.

These textures are consistent with the temperature-dependent phase changes observed by XRD. At lower temperatures, particle contacts and surfaces are modified while recognisable spheres persist. At 800 °C, agglomeration becomes more extensive, and at 900 °C, pronounced consolidation is consistent with sintering in the sodium-bearing system.

The EDX spot analyses (Table 3) record the chemical counterpart of these changes. The Na Kα peak is absent from the feed, weak at 400 °C, moderate at 600 °C and strong at 800 and 900 °C, which tracks the progressive uptake of sodium by the aluminosilicate particles and the formation of $NaAlSiO_4$. Over the same sequence, the Al/Si atomic ratio of the analysed particles decreases from 0.63 in the feed to 0.60 at 800 °C and 0.49 at 900 °C, and Ca increases from about 3 wt% to 5.2–5.5 wt%. An Al/Si ratio below the value of 1 expected for $NaAlSiO_4$ shows that the reacted particles also contain silica-rich material, such as residual quartz, glass or sodium silicate retained after washing. Retained sodium silicate would contribute to the dilution effects considered in Section 3.5.1.

3.5. Behaviour of the REEs and associated elements

3.5.1. Concentration changes and mass effects

The measured concentrations are presented in Table 5. Relative to the feed, the sum of detected REEs including Sc changed by −0.5%, +1.5%, +7.1% and −9.9% at 400, 600, 800 and 900 °C, respectively. Na incorporation, dissolution of soluble material during washing and the resulting changes in residue mass all influence these values. Fig. 6 compares the measured concentration factors with the mass-effect bounds derived in Section 2.5 (0.91–1.43). At 400–800 °C, La, Ce, Y and Ba lie within these bounds, and their small increases (La + Ce +5%, +8% and +10%) are consistent with partial removal of silica as soluble sodium silicate. At 900 °C, La + Ce (−16%) and Ba (−11%) lie slightly below the lower bound, consistent with retention of some sodium-bearing material in the residue (Section 3.4). Element-specific behaviour is therefore assessed on a mass-independent basis in Section 3.5.2.

Table 5. Element concentrations (mg/kg of digested solid) in the feed and the Na_2CO_3-roasted (1:1) and washed products, determined by ICP-MS after HNO_3–HCl–HF microwave digestion.

Element	**Feed**	**400 °C**	**600 °C**	**800 °C**	**900 °C**
Sc	62.02	56.23	55.69	76.20	99.79
Y	47.20	44.09	43.46	51.41	44.91
La	94.47	98.67	102.04	103.69	78.79
Ce	220.98	232.72	239.00	242.87	185.75
Pr	4.42	3.78	3.58	2.92	nd
Nd	44.69	36.86	38.05	33.36	20.09
Gd	1.08	0.83	0.89	nd	nd
Dy	1.72	1.18	1.13	nd	nd
ΣREE (incl. Sc)	476.6	474.4	483.8	510.5	429.3
ΣREY (excl. Sc)	414.6	418.1	428.2	434.3	329.5
ΣLREE (La–Nd)	364.6	372.0	382.7	382.8	284.6
Change in ΣREE vs. feed (%)	–	−0.5	+1.5	+7.1	−9.9
Ba	1056.68	1082.34	1117.33	1166.87	943.71
Sr	1410.08	1219.10	1241.47	1263.34	964.74
Rb	37.09	32.58	31.69	27.64	31.02
Th	28.00	26.01	25.53	25.22	12.71
U	3.14	1.23	1.20	1.77	nd
Ce/La	2.34	2.36	2.34	2.34	2.36

nd = below the instrumental detection limit. Sm, Eu, Tb and Ho–Lu were not detected in any sample.

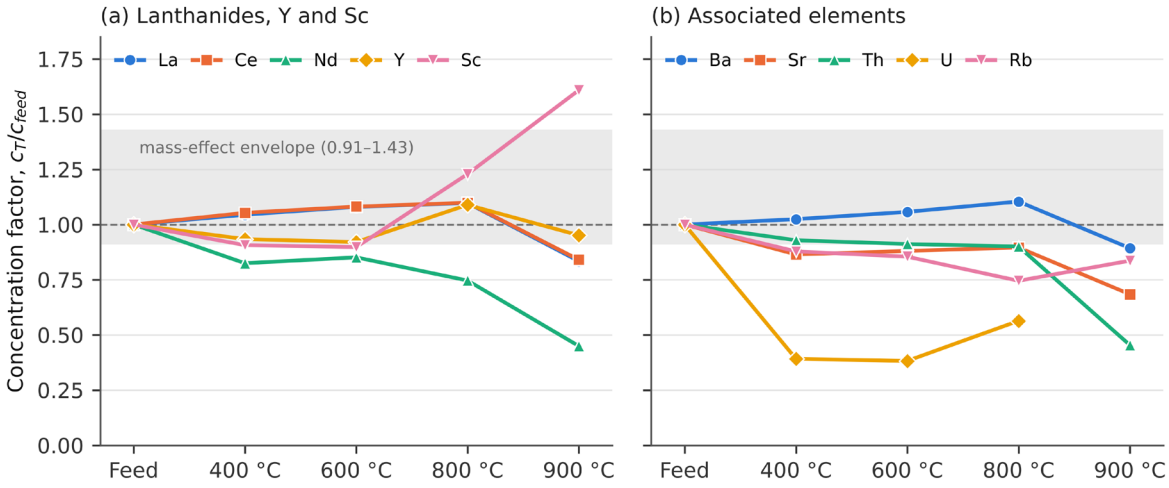

Fig. 6. Concentration factor (concentration in the washed product divided by that in the feed) for (a) lanthanides, Y and Sc and (b) associated elements. The grey band is the range attributable to mass effects alone (0.91–1.43; Section 2.5). U was not detected at 900 °C.

3.5.2. Element-specific behaviour

Normalisation to La + Ce (Eq. 3; Fig. 7) provides a comparison of element ratios independent of a common concentration scaling factor. The Ce/La ratio varied only from 2.34 to 2.36 across the feed and roasted products, and Ba showed a similar relative pattern. La, Ce and Ba therefore behaved coherently across the treatments. Other elements show larger relative changes, which reflect washing, redistribution between phases or analytical matrix effects, as discussed below.

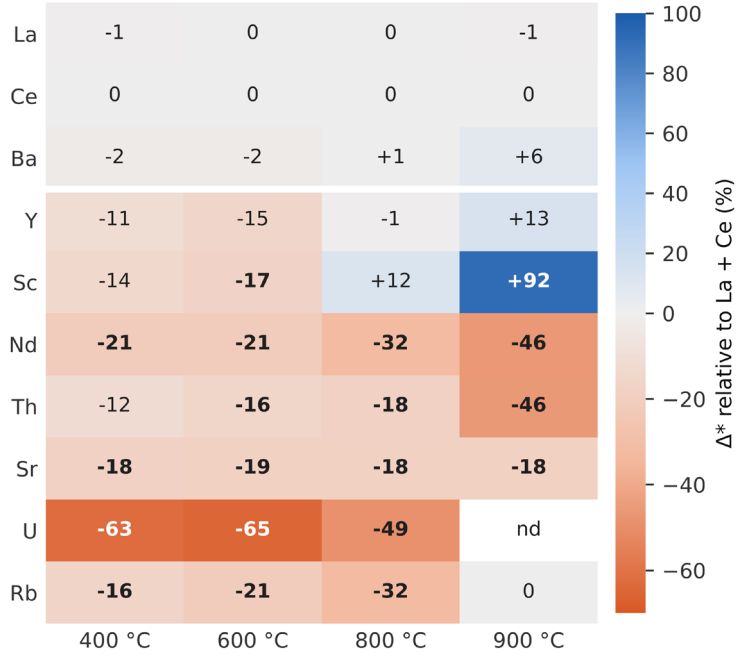

Fig. 7. Ratio-normalised change Δ* (Eq. 3) of each element relative to La + Ce, compared with the feed. Values with $|\Delta^*| \geq 15\%$ are shown in bold; values below 15% are not interpreted (Section 2.5). nd = not detected.

U concentrations relative to La + Ce were 49–65% lower in the roasted products, and U was below detection at 900 °C. The decrease is already fully developed at 400 °C, where the crystalline assemblage is unchanged, and is most likely explained by dissolution of U(VI) as soluble uranyl carbonate complexes in the Na_2CO_3-rich wash liquor, the chemistry that underlies alkaline carbonate leaching of uranium ores (Merritt, 1971).

The Sr/(La + Ce) ratio was 18–19% lower in all roasted products than in the feed. Because the decrease is independent of temperature and mineralogy, it most probably reflects the washing step common to all roasted products.

Rb ratios decreased by 16–32% at 400–800 °C but returned to the feed value at 900 °C. This pattern is consistent with partial removal of Rb released from the glass during washing at lower temperatures and its incorporation in the $NaAlSiO_4$ framework at 900 °C, since the large cation sites of nepheline accommodate K and other large alkali ions.

Th concentrations relative to La + Ce decreased by 46% at 900 °C, coinciding with the most extensive phase transformation. Because Th commonly accompanies the LREEs in phosphate minerals, this suggests that a Th-bearing host was attacked at 900 °C and that part of the released Th was removed during washing, where Th, like U, can form carbonate complexes.

Nd showed larger relative concentration differences than La and Ce, already at 400 °C where the mineralogy was unchanged. Because Nd shares its principal hosts with La and Ce, the Nd trend is not interpreted mechanistically.

Sc concentrations increased relative to La + Ce at 800 and 900 °C, tracking the formation of $NaAlSiO_4$. Sc is monoisotopic (m/z 45) and is subject to matrix-dependent polyatomic interferences from Si-, Ca- and C-based ions (May and Wiedmeyer, 1998); the increase is therefore attributed to the changing digest matrix rather than to Sc enrichment.

3.6. Linking mineralogy, REE occurrence and roasting response

Fig. 8 brings together the phase, morphological and chemical observations. In Regime I (400–600 °C), the crystalline assemblage and the spherical morphology of the feed persist, and the main element-specific changes (U and Sr) do not depend on temperature and may be related to the washing step. The glass and mullite, which are likely to host or encapsulate much of the REE inventory, are not transformed, so no improvement in acid accessibility would be expected from these treatments, in line with the poor performance of Na_2CO_3 at 450 °C reported by Taggart et al. (2018). Regime II (800 °C) marks the onset of $NaAlSiO_4$ formation and particle

agglomeration, but the conversion is partial. Only in Regime III (900 °C) is the crystalline acid-resistant framework extensively converted to $NaAlSiO_4$, which is the mineralogical precondition for acid access to the REE hosts dispersed in or encapsulated by that framework.

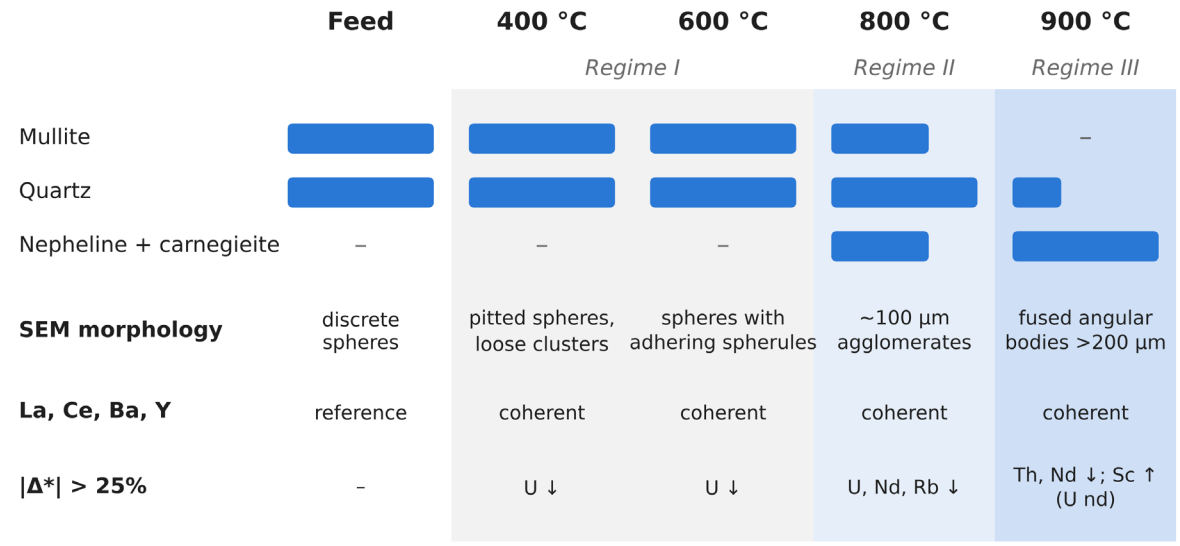

Fig. 8. Summary of the phase assemblage (bar length indicates relative XRD intensity, qualitative), morphology and element behaviour of the feed and the roasted products, defining three temperature regimes. Δ* is the ratio-normalised change relative to La + Ce (Eq. 3).

Across these treatments, La and Ce maintained a nearly constant ratio, whereas several other elements exhibited larger relative changes. These observations show that the two dominant REEs behaved similarly through roasting and washing. The 900 °C treatment yields a substantially transformed mineralogical matrix dominated by acid-soluble $NaAlSiO_4$, which provides a favourable feed for acid leaching.

4. Conclusions

(1) The investigated CFA contains 60.1 wt% SiO_2, 16.7 wt% Al_2O_3, 10.2 wt% Fe_2O_3 and 6.9 wt% CaO. Quartz and mullite were identified as the principal crystalline phases. The feed contains 414.6 mg/kg detected REY excluding Sc, and 62.0 mg/kg Sc.

(2) The feed mineralogy, microchemistry and Th content are consistent with REEs dispersed in aluminosilicate glass, enclosed in accessory phosphate grains and associated with Fe-bearing phases.

(3) At 400 and 600 °C, quartz and mullite remained the principal detected crystalline phases. Nepheline and carnegieite appeared at 800 °C. At 900 °C, mullite reflections were no longer

detected, quartz reflections were substantially diminished and extensive sintering was observed.

(4) The Ce/La ratio remained close to 2.35 across the feed and treated products, and La, Ce and Ba behaved coherently, indicating similar behaviour of the major REEs through roasting and washing.

(5) U and Sr decreased at all roasting temperatures, consistent with removal during washing; Th decreased most strongly at 900 °C, coinciding with the extensive phase transformation; and the apparent Sc increase is attributed to matrix-dependent interference at m/z 45.

(6) Among the temperatures investigated, 900 °C produced the most extensive mineralogical transformation, converting the crystalline mullite–quartz assemblage into acid-soluble $NaAlSiO_4$, and is the preferred pretreatment condition for subsequent acid leaching.

CRediT authorship contribution statement

Nomsa P. Baloyi and Tintswalo B.Z. Baloyi: Conceptualization, Methodology, Investigation, Formal analysis, Writing – original draft, Writing – review & editing.

Declaration of competing interest

The authors declare that they have no known competing financial interests or personal relationships that could have appeared to influence the work reported in this paper.

Declaration of generative AI and AI-assisted technologies in the manuscript preparation process

During the preparation of this work the authors used copilot in order to improve the structure, language and presentation of the manuscript and to prepare figures from the experimental data.

Data availability

Data will be made available on request.

Acknowledgements

The authors acknowledge the University of Johannesburg for SEM-EDX, XRF and XRD facilities, and for analytical services. We are gratefully acknowledges the University of Johannesburg's Accelerated Academic Mentorship Programme (AAMP) for sponsoring conference attendance and for funding the experimental work and analyses reported in this study.

References

ASTM International, 2025. ASTM C618-25, Standard Specification for Coal Ash and Raw or Calcined Natural Pozzolan for Use in Concrete. ASTM International, West Conshohocken, PA.

Balaram, V., 2019. Rare earth elements: A review of applications, occurrence, exploration, analysis, recycling, and environmental impact. Geosci. Front. 10, 1285–1303.

Cao, S., Zhou, C., Pan, J., Liu, C., Tang, M., Ji, W., Hu, T., Zhang, N., 2018. Study on influence factors of leaching of rare earth elements from coal fly ash. Energy Fuels 32, 8000–8005. https://doi.org/10.1021/acs.energyfuels.8b01316

Cornelius, M.-L.U., Ameh, A.E., Eze, C.P., Fatoba, O., Sartbaeva, A., Petrik, L.F., 2021. The behaviour of rare earth elements from South African coal fly ash during enrichment processes: Wet, magnetic separation and zeolitisation. Minerals 11, 950. https://doi.org/10.3390/min11090950

Dai, S., Finkelman, R.B., 2018. Coal as a promising source of critical elements: Progress and future prospects. Int. J. Coal Geol. 186, 155–164.

Eskom, 2024. Eskom leads sustainable road construction by using recycled coal ash as an alternative to concrete. Media statement, 26 September 2024. https://www.eskom.co.za/eskom-leads-sustainable-road-construction-by-using-recycled-coal-ash-as-an-alternative-to-concrete/

European Commission, 2020. Critical Raw Materials for Strategic Technologies and Sectors in the EU – A Foresight Study. Publications Office of the European Union, Luxembourg.

Fu, B., Hower, J.C., Zhang, W., Luo, G., Hu, H., Yao, H., 2022. A review of rare earth elements and yttrium in coal ash: Content, modes of occurrences, combustion behavior, and extraction methods. Prog. Energy Combust. Sci. 88, 100954. https://doi.org/10.1016/j.pecs.2021.100954

King, J.F., Taggart, R.K., Smith, R.C., Hower, J.C., Hsu-Kim, H., 2018. Aqueous acid and alkaline extraction of rare earth elements from coal combustion ash. Int. J. Coal Geol. 195, 75–83. https://doi.org/10.1016/j.coal.2018.05.009

Kolker, A., Scott, C., Hower, J.C., Vazquez, J.A., Lopano, C.L., Dai, S., 2017. Distribution of rare earth elements in coal combustion fly ash, determined by SHRIMP-RG ion microprobe. Int. J. Coal Geol. 184, 1–10.

Liu, C., Zhao, A., Ye, X., Zhao, Z., Zhang, T., Yang, X., Qin, Y., 2024. Effect of Na_2CO_3 roasting activation on acid leaching property of fly ash. J. Wuhan Univ. Technol.-Mater. Sci. Ed. 39, 1613–1620. https://doi.org/10.1007/s11595-024-3031-2

Liu, P., Huang, R., Tang, Y., 2019. Comprehensive understandings of rare earth element (REE) speciation in coal fly ashes and implication for REE extractability. Environ. Sci. Technol. 53, 5369–5377. https://doi.org/10.1021/acs.est.9b00005

May, T.W., Wiedmeyer, R.H., 1998. A table of polyatomic interferences in ICP-MS. At. Spectrosc. 19(5), 150–155. https://doi.org/10.46770/AS.1998.05.002

Merritt, R.C., 1971. The Extractive Metallurgy of Uranium. Colorado School of Mines Research Institute, Golden, CO.

Pan, J., Zhou, C., Tang, M., Cao, S., Liu, C., Zhang, N., Wen, M., Luo, Y., Hu, T., Ji, W., 2019. Study on the modes of occurrence of rare earth elements in coal fly ash by statistics and a sequential chemical extraction procedure. Fuel 237, 555–565. https://doi.org/10.1016/j.fuel.2018.09.139

Rerani, V.P., Mabowa, H.M., Wagner, N.J., 2024. Characterisation of rare earth element-bearing mineral phases present in South African coal ash using Mineral Liberation Analysis. Fuel 368, 131661. https://doi.org/10.1016/j.fuel.2024.131661

Rudnick, R.L., Gao, S., 2003. Composition of the continental crust, in: Holland, H.D., Turekian, K.K. (Eds.), Treatise on Geochemistry, Vol. 3. Elsevier, Oxford, pp. 1–64.

Seredin, V.V., Dai, S., 2012. Coal deposits as potential alternative sources for lanthanides and yttrium. Int. J. Coal Geol. 94, 67–93.

Taggart, R.K., Hower, J.C., Dwyer, G.S., Hsu-Kim, H., 2016. Trends in the rare earth element content of U.S.-based coal combustion fly ashes. Environ. Sci. Technol. 50, 5919–5926.

Taggart, R.K., Hower, J.C., Hsu-Kim, H., 2018. Effects of roasting additives and leaching parameters on the extraction of rare earth elements from coal fly ash. Int. J. Coal Geol. 196, 106–114. https://doi.org/10.1016/j.coal.2018.06.021

Tang, M., Zhou, C., Pan, J., Zhang, N., Liu, C., Cao, S., Hu, T., Ji, W., 2019. Study on extraction of rare earth elements from coal fly ash through alkali fusion – Acid leaching. Miner. Eng. 136, 36–42. https://doi.org/10.1016/j.mineng.2019.01.027

U.S. Department of Energy (DOE), 2017a. Report on Rare Earth Elements from Coal and Coal Byproducts. U.S. DOE, Washington, DC.

U.S. Department of Energy (DOE), 2017b. High concentrations of rare earth elements found in American coal basins. News release, 29 November 2017. https://www.energy.gov/node/3038612

Wagner, N.J., Matiane, A., 2018. Rare earth elements in select Main Karoo Basin (South Africa) coal and coal ash samples. Int. J. Coal Geol. 196, 82–92. https://doi.org/10.1016/j.coal.2018.06.020